The Astrophysical Journal, 742:82 (10pp), 2011 December 1 doi:10.1088/0004-637X/742/2/82


# ELECTRON ACCELERATION ASSOCIATED WITH SOLAR JETS

Säm Krucker[1,2], E. P. Kontar[3], S. Christe[4], L. Glesener[1,5], and R. P. Lin[1,5]
[1] Space Sciences Laboratory, University of California, Berkeley, CA 94720-7450, USA; krucker@ssl.berkeley.edu
[2] Institute of 4D Technologies, School of Engineering, University of Applied Sciences Northwestern Switzerland, 5210 Windisch, Switzerland
[3] Department of Physics and Astronomy, University of Glasgow, Glasgow G12 8QQ, UK
[4] Heliophysics Science Division, NASA Goddard Space Flight Center Greenbelt, MD 20771-0001, USA
[5] Department of Physics, University of California, Berkeley, CA 94720-7300, USA
*Received 2011 June 16; accepted 2011 August 18; published 2011 November 8*

## ABSTRACT

This paper investigates the solar source region of supra-thermal (few keV up to the MeV range) electron beams observed near Earth by combining in situ measurements of the three-dimensional Plasma and Energetic Particles experiment on the *WIND* spacecraft with remote-sensing hard X-ray observations by the *Reuven Ramaty High Energy Solar Spectroscopic Imager*. The in situ observations are used to identify events, and the hard X-ray observations are then searched for signatures of supra-thermal electrons radiating bremsstrahlung emission in the solar atmosphere. Only prompt events detected above 50 keV with a close temporal correlation between the flare hard X-ray emission and the electrons seen near Earth are selected, limiting the number of events to 16. We show that for 7 of these 16 events, hard X-ray imaging shows three chromospheric sources: two at the footpoints of the post-flare loop and one related to an apparently open field line. The remaining events show two footpoints (seven events, four of which show elongated sources possibly hiding a third source) or are spatially unresolved (two events). Out of the 16 events, 6 have a solar source region within the field of view of the *Transition Region and Corona Explorer* (*TRACE*). All events with *TRACE* data show EUV jets that have the same onset as the hard X-ray emission (within the cadence of tens of seconds). After the hard X-ray burst ends, the jets decay. These results suggest that escaping prompt supra-thermal electron events observed near Earth are accelerated in flares associated with reconnection between open and closed magnetic field lines, the so-called interchange reconnection scenario.

*Key words:* Sun: flares – Sun: particle emission – Sun: X-rays, gamma rays

*Online-only material:* color figures

## 1. INTRODUCTION

The release of magnetic energy in the solar atmosphere is observed to occur very impulsively, producing solar flares and coronal mass ejections (CMEs). A significant fraction of the released energy goes into the acceleration of particles (see review by Benz 2008). While particle acceleration at the CME shocks is understood in some detail, particle acceleration during the solar flares is still very much debated. Furthermore, the escape of flare-accelerated electrons from the flare site into interplanetary space is poorly understood (e.g., Klein et al. 2008).

The most direct diagnostics of flare-accelerated electrons are hard X-ray observations of their bremsstrahlung emissions (e.g., Dennis et al. 2011). Solar flare bremsstrahlung emission is proportional to the surrounding plasma density and hence is generally strongest from the chromosphere. These sources outline footpoints (e.g., Hoyng et al. 1981; Masuda et al. 2001; Liu et al. 2007; Krucker et al. 2011) of magnetic field lines connected to the coronal acceleration region. Hard X-ray sources in the corona are likely always present as well (e.g., Krucker & Lin 2008), but are much fainter, and therefore difficult to observe in the presence of the strong footpoint sources (see review by Krucker et al. 2008). Coronal densities are generally low and collisional losses do not significantly lower the energy of electrons above ∼10 keV. Flare-accelerated electrons on magnetic field lines with access to interplanetary space (so-called open field lines) are therefore able to escape the Sun. In situ observations of these escaping electrons provide a second, independent diagnostic by directly measuring the electron distribution function (e.g., Lin 1985). Escaping electrons can be traced by radio emissions produced by the beam-driven Langmuir turbulence, providing a further diagnostic (e.g., Ginzburg & Zhelezniakov 1958; Zaitsev et al. 1972; Melrose 1990; Muschietti 1990).

Some events show a clear temporal correlation between the hard X-ray producing electrons and the escaping electrons seen in radio and in situ measurements (e.g., Kane 1981; Benz et al. 2001; Klein et al. 2005; Benz et al. 2005). The electron spectra of these prompt events at 1 AU correlate well with the spectra of the hard X-ray producing electrons (Krucker et al. 2007b), strongly suggesting a common acceleration mechanism. For other events, there is no temporal correlation, with the escaping electrons being delayed relative to the hard X-ray bursts (e.g., Krucker et al. 1999; Haggerty & Roelof 2002; Klassen et al. 2002). Delayed events are speculated to be shock-accelerated (e.g., Krucker et al. 1999; Haggerty & Roelof 2002). Common to all events is that the number of escaping electrons is much smaller (typically 0.5%) than the number of electrons needed to produce the observed hard X-ray emissions (e.g., Lin & Hudson 1971).

The most discussed flare topology involving open field lines is interchange reconnection (e.g., Parker 1973; Crooker & Webb 2006; Baker et al. 2009) where emerging magnetic loops reconnect with open field lines (the term "interchange" refers to the changes of magnetic elements in the photosphere from closed to open to the interplanetary space). Such magnetic field reconfigurations can lead to plasma heating and particle acceleration, while the presence of the open magnetic field lines allow energetic electrons to escape into interplanetary space. Candidate mechanisms for electron acceleration include reconnection electric fields, shocks produced by the reconnection outflow, collapsing traps, collapsing magnetic islands, and turbulence

(for a review see Zharkova et al. 2011). Whether electrons are accelerated directly on open field lines or escape from closed fields along newly reconnected field lines remains an open question. Within the interchange reconnection model, precipitating electrons that radiate bremsstrahlung emission in the hard X-ray range are expected to produce three footpoint sources in the chromosphere: two at the footpoints of the newly formed flare loop and a third one at the footpoint of the newly opened field line.

Strong observational evidence for the interchange reconnection model comes from thermal emissions seen in soft X-ray and EUV. Imaging observations at these wavelengths show plasma ejections along apparently open field lines located in close proximity to post-flare loops (e.g., Shibata et al. 1992; Shimojo et al. 1996; Kim et al. 2007). These ejections are well collimated and are called soft X-ray and EUV jets. Further evidence that these jets are indeed reaching interplanetary space is that they are found to be correlated with ejecta (sometimes referred to as narrow CMEs or white light jets) seen in scattered white light observed by coronographs (Wang & Sheeley 2002). More recently, soft X-ray jets have also been seen from the quiet corona and polar regions (Savcheva et al. 2007; Cirtain et al. 2007); indicating that interchange reconnection is a common process. It has been speculated that the large number of small interchange reconnection events could contribute to the solar wind acceleration (e.g., Axford & McKenzie 1992; Fisk 2003; Cranmer & van Ballegooijen 2010).

Evidence for electron acceleration in the interchange reconnection model comes from type III radio bursts that are found to be cospatial with the soft X-ray jet (Aurass et al. 1994; Kundu et al. 1995; Raulin et al. 1996). To detect the radio type III producing electrons through their hard X-ray emission would give us a strong diagnostic tool, but emission is expected to be extremely faint (Saint-Hilaire et al. 2009). Krucker et al. (2008b) reported a first detection at the limit of *Reuven Ramaty High Energy Solar Spectroscopic Imager* (*RHESSI*) sensitivity. Bain & Fletcher (2009) reported hard X-ray emission from a jet-like feature in the corona associated with a two-ribbon flare and a gradual solar energetic particle event. They found in addition to the chromospheric footpoint sources an almost equally strong extended coronal source with a power-law spectrum indicating the presence of non-thermal electrons in the corona. However, the number of non-thermal (>30 keV) electrons needed to produce the observed coronal source (several times $10^{35}$) is three orders of magnitude larger than the typical number of escaping electrons (several times $10^{32}$; e.g., Lin & Hudson 1971). Therefore, type III burst producing electrons cannot account for the observed coronal source reported by Bain & Fletcher (2009). Similarly, strong coronal hard X-ray sources that move outward such as seen by Bain & Fletcher (2009) have been reported previously (Kane et al. 1992; Hudson et al. 2001; Krucker et al. 2007a). These emissions are interpreted as bremsstrahlung emission from energetic electrons trapped in magnetic structures that are ejected as part of the CME.

Soft X-ray jet events have also been observed to be correlated with $^3$He-rich solar energetic particle events (Wang et al. 2006a; Pick et al. 2006; Nitta et al. 2008) indicating that not only electrons, but also ions are accelerated. However, timing arguments derived from in situ ion observations suggest that ion acceleration in these events occurs about an hour after flare and jet onset (Wang et al. 2006b), suggesting that ion acceleration is not directly associated to the jet. Further evidence for particle acceleration in jet events is reported by several studies reporting jet emission in association with hard X-ray microflares showing emission from chromospheric footpoints (e.g., Christe et al. 2008; Chifor et al. 2008; Nitta et al. 2008), but no statistical study has been done so far.

In this paper, we present a statistical survey of 16 prompt events simultaneously observed by the three-dimensional Plasma and Energetic Particles experiment on the *WIND* (Lin et al. 1995) and by the *RHESSI* (Lin et al. 2002) to systematically study the solar source region of the electron beams observed near Earth. In addition to *RHESSI* hard X-ray images, imaging observations from *Solar and Heliospheric Observatory* (*SOHO*) Michelson Doppler Imager (MDI) (Scherrer et al. 1995) and *Transition Region and Corona Explorer* (*TRACE*; Handy et al. 1999) are used to compare the solar source region with the interchange reconnection geometry.

## 2. OBSERVATIONS AND DATA ANALYSIS

The survey presented here consists of the same 16 prompt events selected by Krucker et al. (2007b). For these events, the first arriving electrons appear to travel scatter-free (ballistic) with a solar release occurring at the time of the hard X-ray burst (see Krucker et al. 2007b for details). The associated soft X-ray flare emissions are all found to be short with typical durations of 10 minutes. All events show radio type III bursts starting in the meter wavelength range. The total duration of the type III bursts at the highest frequencies is similar to the hard X-ray burst duration (Figure 1). However, the time evolution of individual bursts in radio and hard X-rays does not always match. This difference could be due to the different electron energies involved in producing the two emissions (typically >20 keV for hard X-rays and ~1–30 keV for the radio waves). A further difference is that the radio emission is only produced at times when the electron distribution is unstable and when the wave growth rate is faster than any simultaneously acting damping, while bremsstrahlung emissions are always produced, only scaling with the ambient density. Krucker et al. (2007b) showed that for this set of events the electron spectra measured near Earth correlate with the hard X-ray photon spectra observed at the Sun, suggesting a common origin. The selected events therefore represent the simplest event geometry of acceleration of electrons in the solar corona with access to interplanetary space. A single accelerator is expected to produce both downward going and escaping electrons. In the following, imaging results of the solar source region are discussed.

### 2.1. X-Ray Imaging

For our statistical study of non-thermal bremsstrahlung sources, images integrated over the total duration of the main hard X-ray peak are considered (see Table 1). The time evolution of images of the few events with very good counting statistics will be discussed in a future paper. The energy range used to reconstruct the non-thermal images is selected from the spectral fits from Krucker et al. (2007b). Care has been taken to ensure that the selected energy range mostly contains non-thermal emissions (i.e., power-law spectrum), and that also the majority of counts in the non-thermal range are included. The lower end of the energy range for imaging the non-thermal component is set to the value where the thermal fit is 10% of the total emission (see Krucker et al. 2007b for an example of a photon spectrum). This ensures that the non-thermal images presented in this paper have thermal contamination below the 10% level and contain most of the non-thermal counts. The thermal images

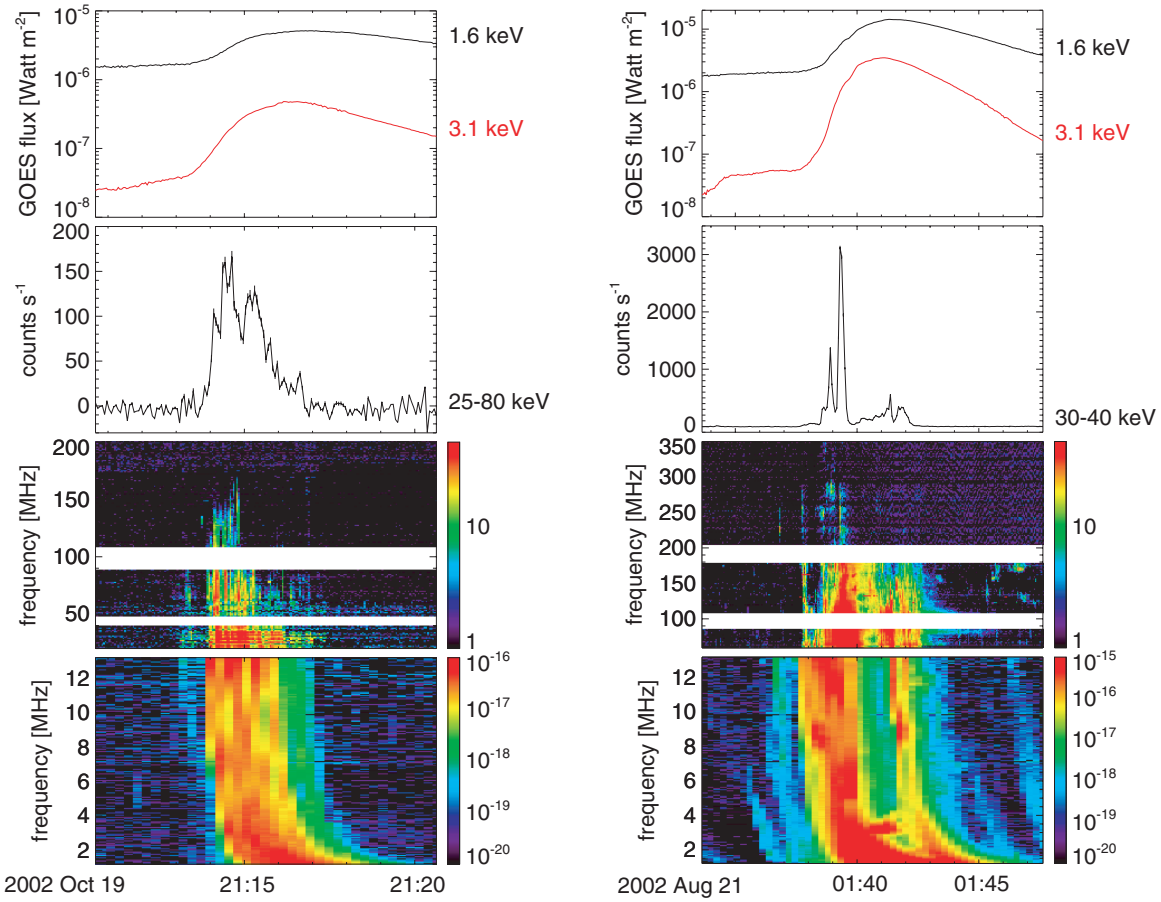


**Figure 1.** Timing of X-ray and radio emission for two events. From top to bottom, the panel shows *GOES* soft X-ray and *RHESSI* hard X-ray light curves, radio spectrogram from ground-based observatories (Culgoora), and radio observations from the WAVE instrument (Bougeret et al. 1995) on board the *WIND* spacecraft. (A color version of this figure is available in the online journal.)

**Table 1**
Hard X-ray Flares Associated with Supra-thermal Electron Events Seen Near Earth

| No. | HXR Peak Time | *GOES* Class | Location | *TRACE* | $N_f$[a] | $P_{1AU}$[b] | $B_{fp}$[c] Range (G) | Average $B_{fp}$[c] (G) |
|---|---|---|---|---|---|---|---|---|
| 1 | 2002 Feb 20 11:06:00–11:06:20 | C7.5 | N15W77 | ... | 3 | Pos | ... | ... |
| 2 | 2002 Apr 14 22:24:51–22:26:00 | C7.2 | N18W74 | ... | 1+ | Pos | ... | ... |
| 3 | 2002 Apr 25 05:55:11–05:55:50 | C2.5 | S19W08 | ... | 2+ | Pos | ... | ... |
| 4 | 2002 Aug 19 21:00:25–21:01:16 | M3.1 | S11W33 | 195A | 2+ | Neg | ... | ... |
| 5 | 2002 Aug 20 01:34:11–01:35:23 | M5.0 | S11W35 | 195A | 3 | Neg | −160 to +170 | −10 |
| 6 | 2002 Aug 20 08:25:17–08:25:41 | M3.4 | S07W40 | 195A | 3 | Neg | −730 to +190 | −380 |
| 7 | 2002 Aug 21 01:38:31–01:39:36 | M1.4 | S11W47 | 195A | 3 | Neg | −100 to +230 | +80 |
| 8 | 2002 Oct 19 21:13:54–21:15:36 | C5.0 | S13W48 | ... | 3 | Neg | −200 to 0 | −40 |
| 9 | 2003 Sep 30 08:48:46–08:49:04 | C3.2 | N09W45 | 1600A & 171A | 2 | Neg | ... | ... |
| 10 | 2003 Dec 31 18:22:25–18:22:39 | M1.0 | N10W84 | after 18:35 | 1 | Pos | ... | ... |
| 11 | 2004 Mar 31 20:05:25–20:05:37 | C7.4 | N15W11 | 195A | 3 | Pos | +80 to +800 | +310 |
| 12 | 2004 Oct 30 03:30:00–03:30:56 | M3.3 | N13W20 | ... | 2 | Pos | ... | ... |
| 13 | 2004 Oct 30 16:24:14–16:25:54 | M5.9 | N13W28 | ... | 2 | Pos | ... | ... |
| 14 | 2004 Nov 1 03:18:52–03:19:10 | M1.1 | N12W49 | ... | 3 | Pos | 0 to +180 | +100 |
| 15 | 2005 May 16 02:39:02–02:40:31 | M1.4 | S16E18 | ... | 2+ | Pos | ... | ... |
| 16 | 2005 Nov 24 16:08:26–16:08:46 | B1.6 | S08W82 | ... | 2+ | Pos | ... | ... |

**Notes.**
[a] Number of footpoints, + marks elongated sources.
[b] Polarization of interplanetary magnetic field line at *WIND* spacecraft.
[c] Magnetic field strength (line of sight) in open footpoint.

are taken at the peak time of the thermal emission that immediately follows the main hard X-ray burst. In this way, the thermal emission resulting from heating related to the non-thermal energy input is studied (Neupert effect). The thermal images taken at the same time as the non-thermal images look similar, but the lower counting statistics decrease the image quality.

The thermal and non-thermal images are superposed in Figure 2 for comparison. Three hard X-ray footpoints are seen in

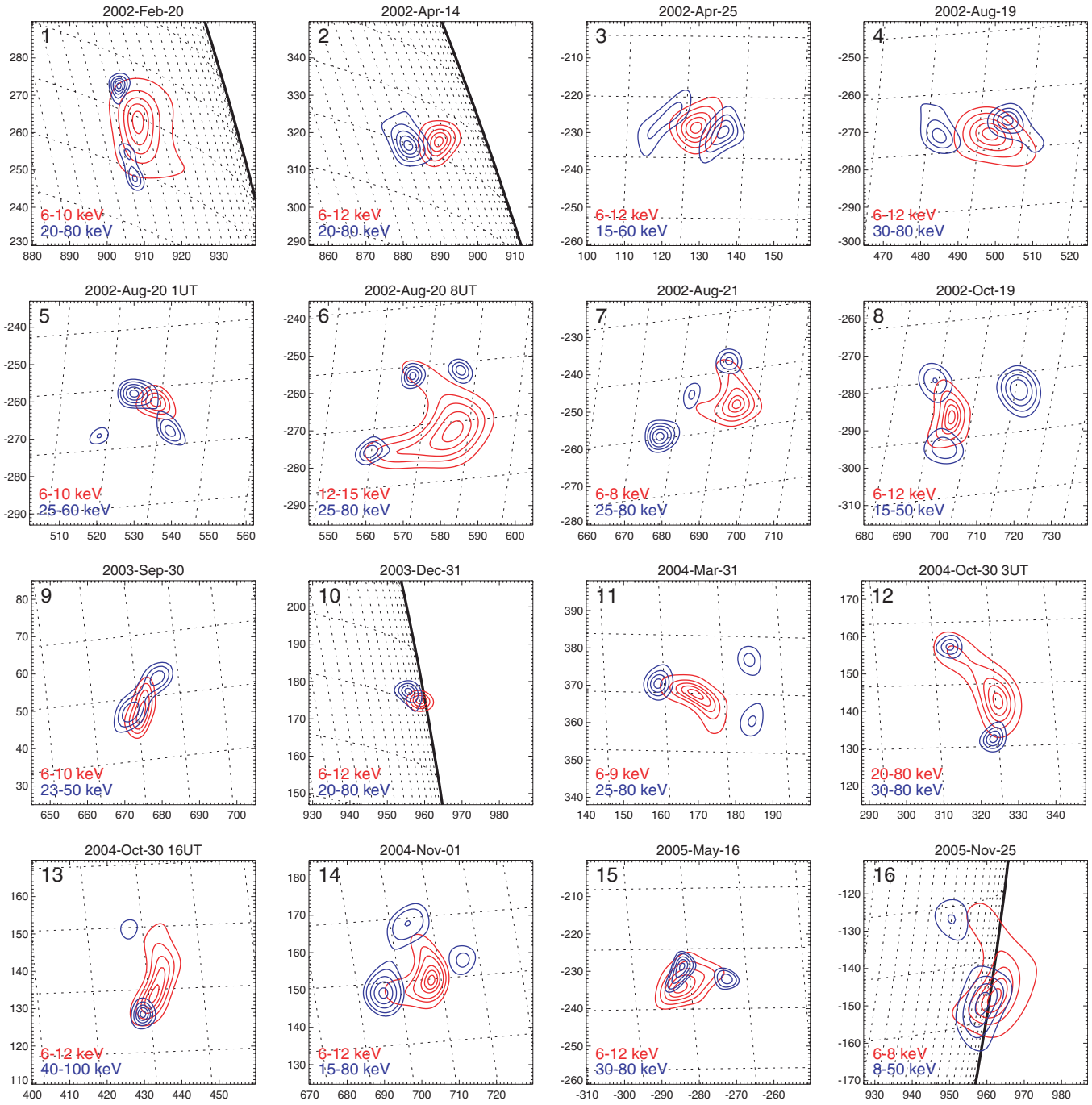


**Figure 2.** Hard X-ray imaging results using *RHESSI* visibilities and the maximum entropy method (Schmahl et al. 2007) of the 16 events listed in Table 1. CLEAN images show qualitatively the same sources (for detailed discussions on *RHESSI* imaging techniques we refer to Hurford et al. 2002 and Dennis & Pernak 2009). Each figure shows thermal X-ray emission in red contours, and non-thermal emission in blue. The contour levels are at 10%, 30%, 50%, 70%, and 90%. Depending on the signal-to-noise ratio of the image, only the higher contour levels are shown.

(A color version of this figure is available in the online journal.)

7 out of the 16 events (Table 1). For these events, two footpoints are from the main flare loop seen in thermal emission. The third source is clearly separated (except possibly for event 1) from the main flare loop and is not associated with the main thermal emission. This is as expected from an interchange reconnection model. The remaining events show only two source (seven events) or are spatially unresolved (two events). A third footpoint could be missed in these events because of (1) insufficient dynamic range (e.g., event 13) or (2) insufficient spatial resolution (e.g., event 10). Four of the seven events with double sources show elongated sources possibly hiding a spatially unresolved third source. However, source motion can produce elongated sources as well (e.g., Qiu et al. 2002; Yang et al. 2009). We are not aware of a statistical study of the number of hard X-ray sources observed in solar flares that would allow us to compare our results. In summary, out of the 14 spatially resolved events, half clearly show three footpoints as expected from the interchange reconnection geometry. For the other events, the limited image quality does not allow us to draw additional conclusions.

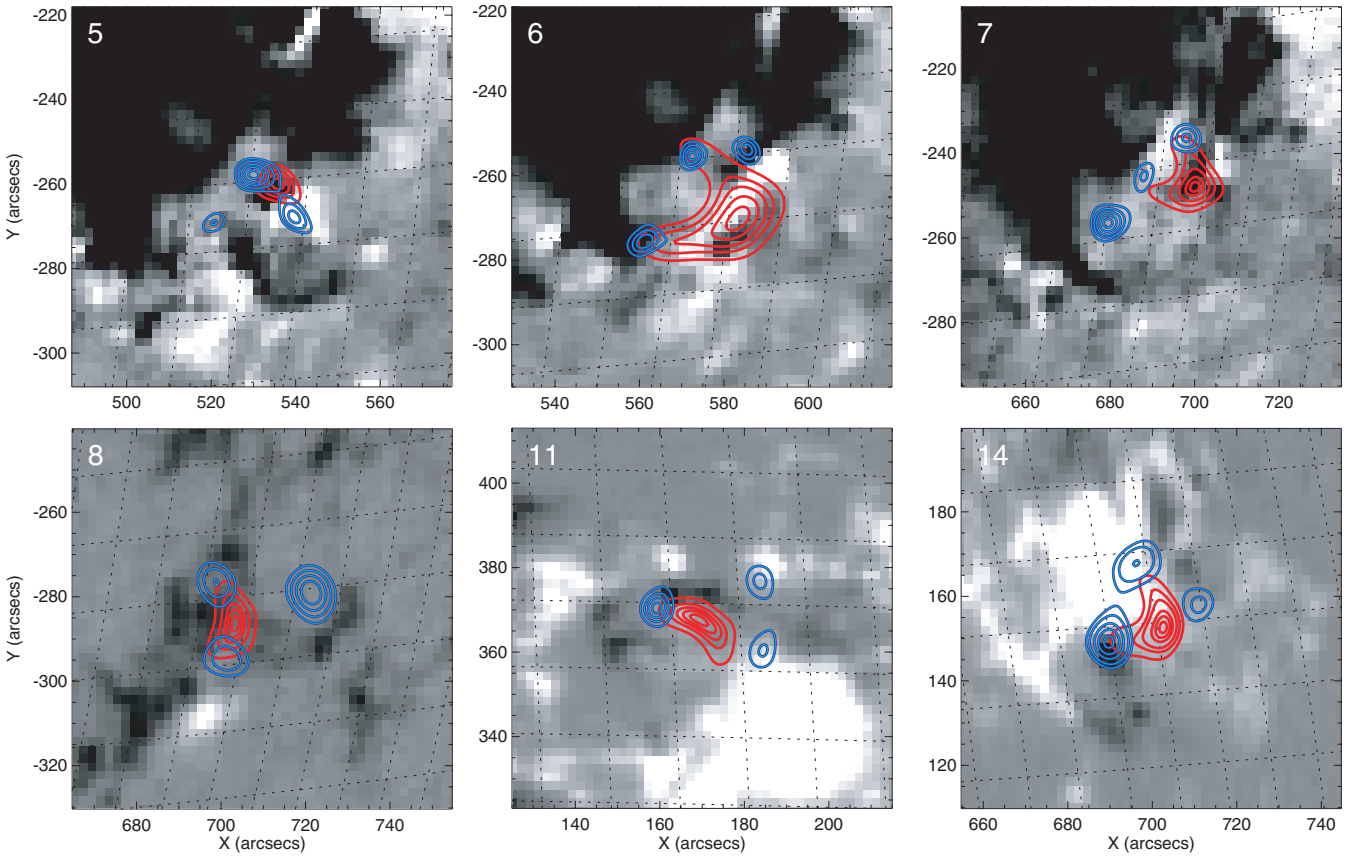


**Figure 3.** Hard X-ray contours shown on MDI line-of-sight magnetograms (gray scale goes from −500 G to +500 G) for six events that clearly show three hard X-ray footpoints. The numbers in the top left corner correspond to the number given in Table 1. Because all events occur relatively far away from disk center, the derived polarity of the magnetic field in the footpoints is inconclusive, except possibly for event 11 (see the text for details).

(A color version of this figure is available in the online journal.)

### 2.2. Polarity of the Open Magnetic Field Lines

A further test for the interchange reconnection geometry is to compare the polarity of the magnetic field in the hard X-ray footpoints to the polarity of the field line that connects the *WIND* spacecraft with the Sun. While the idea of comparing the polarity appears to be straightforward to test, the available line-of-sight magnetograms from *SOHO* MDI make a comparison very difficult. Most of our events occur relatively far away from the disk center (Table 1). Because coronal loops can be significantly inclined relative to the radial direction (e.g., Smith et al. 2003; Aschwanden et al. 2008), the apparent polarity in the line-of-sight measurements can be deceiving.

In the following, the magnetic topology of the events with three hard X-ray footpoints is discussed. From the seven events with three footpoints, we exclude event number 1 because of its proximity to the solar limb. The magnetograms of the remaining events are shown in Figure 3 with the hard X-ray contours from Figure 2 superposed. The largest uncertainty in the alignment is due to the ∼1 deg uncertainty of the roll angle of MDI. For the events shown in Figure 3, this translates to a positional uncertainty along constant radius of less than 5 arcsec. The magnetograms of the selected events show relatively small size structures with size scales down to 5 arcsec. Hence, the roll angle uncertainties further complicate the data analysis. As a consistency check, we first determined the polarity of the two footpoints of the main flare loop expecting to find opposite polarities. However, due to line-of-sight effects and alignment uncertainties, this is not always the case (most clearly seen in event 7 with both ends of the thermal loop rooted in positive polarity). This clearly shows the limitations of the available data. Nevertheless, we estimated a range of magnetic field strength for each hard X-ray source on the apparently open field line within a 5 arcsec circle around the centroid of the hard X-ray source (Table 1). Only events 8, 11, and 14 give the same polarity estimate for all pixels within this range. Nevertheless, also for these events, line-of-sight effects could still possibly reverse the sign. The polarity of the open field line connecting the *WIND* spacecraft with the Sun is given by the arrival direction of the electron event and magnetic field measurements (Table 1). For the events with the most reliable polarity estimate (events 8, 11, and 14), the two polarities agree. However, without vector magnetogram observations, the results of the polarity comparisons are inconclusive. Vector magnetogram measurements from *Hinode* Solar Optical Telescope and *Solar Dynamics Observatory* (*SDO*) should be used in the near future to further study this point. Combined remote-sensing and in situ observations by Solar Orbiter in the inner heliosphere where the magnetic field is mostly radial will greatly simplify these comparisons.

### 2.3. TRACE EUV Observations

We used the *TRACE* database to search for EUV jets associated to our set of events. Out of the six events with *TRACE* coverage, all events show related EUV jets. However, we note that four out of these six events occur in the same active region. This selection bias makes the conclusion that all events

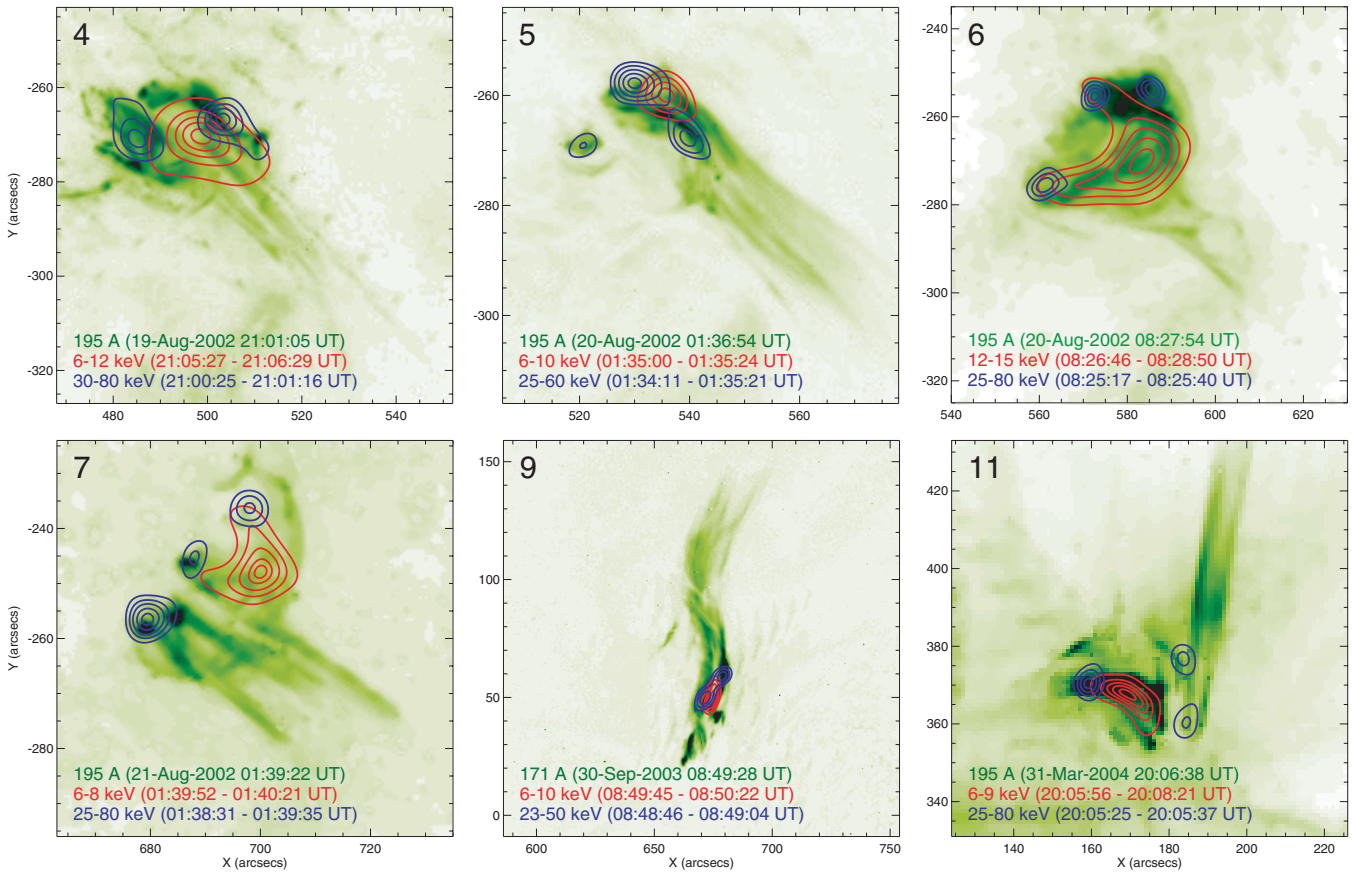


**Figure 4.** Solar source region in hard X-ray and EUV of the six events with *TRACE* observations. For each event, a *TRACE* image (dark is enhanced emission) is shown with the thermal (red) and non-thermal (blue) hard X-ray emission overlaid (cf. Figure 2). The numbers in the top left corner correspond to the number given in Table 1. All events show EUV jets.

(A color version of this figure is available in the online journal.)

with *TRACE* data show jets slightly less convincing. Figure 4 shows the EUV imaging results. Because the absolute pointing of *TRACE* is not accurately known, the uncertainties in the alignment are significant (possibly in the range of 10 arcsec). We used the footpoint location and the location of the post-flare loops to co-align the EUV and hard X-ray images by eye. The association of the third hard X-ray footpoint with the EUV jet is most clearly seen in events 7 and 11 corroborating the interchange reconnection geometry. The EUV images show complex structures with elongated sources in the jet direction. The nature of the elongated structure is not well understood and needs some detailed investigation in the future. The time evolution of the EUV jet relative to the hard X-ray time profile shows a clear temporal correlation (Figure 5), but the relatively low and irregular cadence of the available EUV images makes a detailed comparison difficult. The jets start simultaneously with the hard X-rays within tens of seconds, but tend to last slightly longer with a slower decay.

### *2.4. Hard X-Ray Emission Associated with Jet*

Triggered by the recent paper by Bain & Fletcher (2009), we searched our set of events for coronal hard X-ray emission associated with jets. The images shown in Figure 1 would not reveal such extended sources, because of the expected low brightness of jet-related extended emission. As an example, let us consider emission from three equally bright footpoints (each with a spatial extent of $7'' \times 7''$, i.e., resolved with subcollimator 3) and from a jet ($35'' \times 35''$, i.e., resolved with subcollimator 6) with the same total flux as a single footpoint (i.e., the coronal emission is assumed to be very bright, with 25% of the total flux). Because the jet area is 25 times larger than a single footpoint source, the jet-related emission would only appear on the 4% contour levels in the images of Figure 1, well below the dynamic range of these images. However, with *RHESSI*'s ability to make an image with lower spatial resolution at the scale size of the extended coronal source, we can overcome this problem. In this coarse-resolution image the footpoints are unresolved, appearing as sources of the same size as the coronal source. Hence, in this image, all sources in our example are equally bright. Figure 6 illustrates a new method of making CLEANed images with *RHESSI* of extended sources in the presence of compact footpoint sources. In this new approach, the CLEAN algorithm (Hurford et al. 2002) is run in two steps: first, a fine-resolution image is made and the CLEAN components of the footpoints are obtained. In a second step, the CLEAN components of the footpoints are subtracted from a coarse-resolution backprojection image, and the resulting residual map is CLEANed using the standard software. In this way, we obtain a coarse-resolution image of extended sources (if present) with the footpoint emission subtracted.

To test the new two-step CLEAN algorithm, the event from Bain & Fletcher (2009) is used. Consistent with images shown in Bain & Fletcher (2009), the two-step clean algorithm shows two footpoint sources and an extended coronal source (Figure 6, bottom right). The extended hard X-ray source nicely outlines the extent of the EUV jet. Despite the low brightness of the

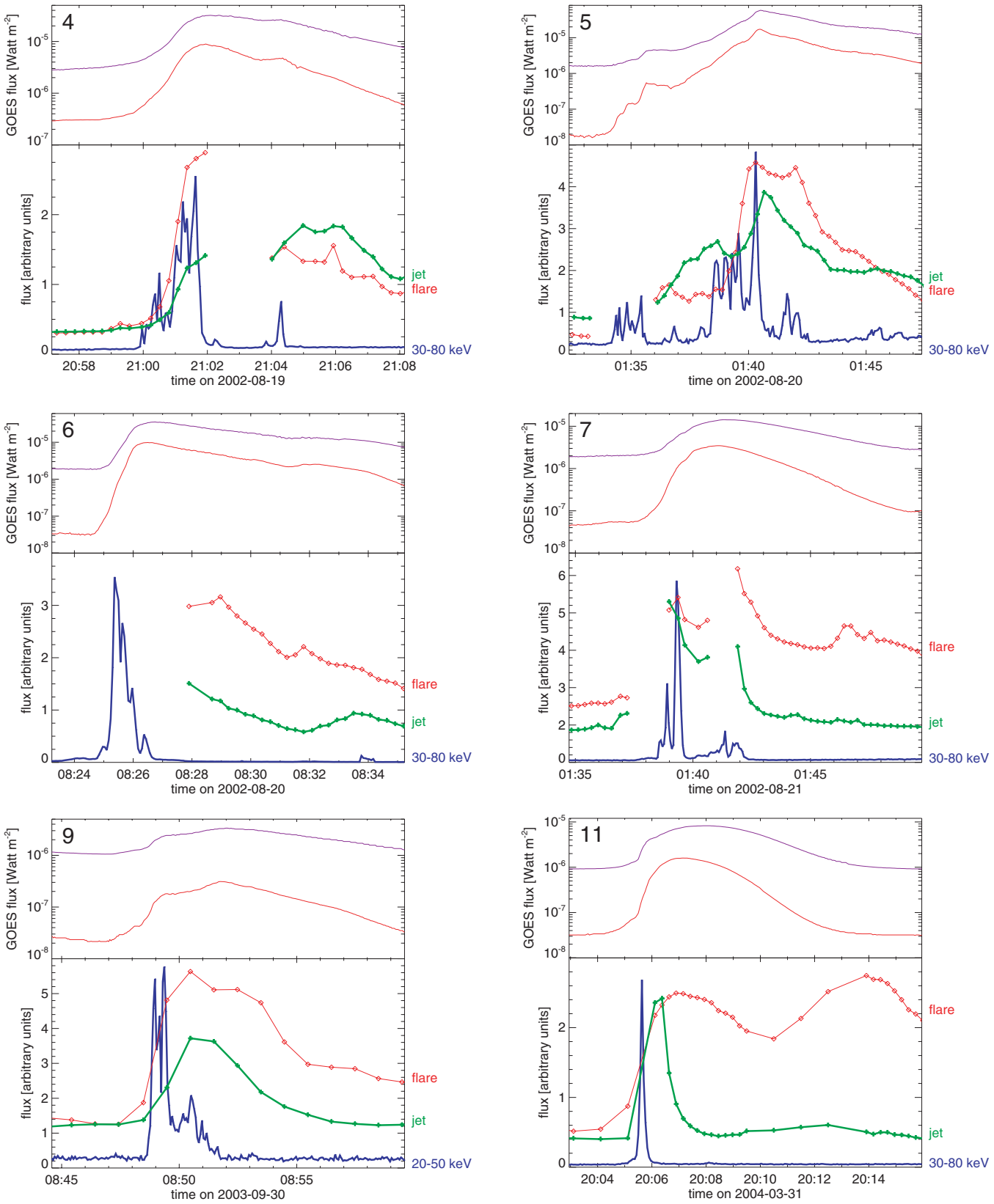


**Figure 5.** Temporal evolution of the six events with *TRACE* observations. For each event, the *GOES* soft X-ray flux (top panel), the time profile in non-thermal hard X-ray (bottom panel, blue), the EUV emission of the jet (bottom panel, green), and the EUV emission of the flare (bottom panel, red) are shown. The numbers in the top left corner correspond to the number given in Table 1.

(A color version of this figure is available in the online journal.)

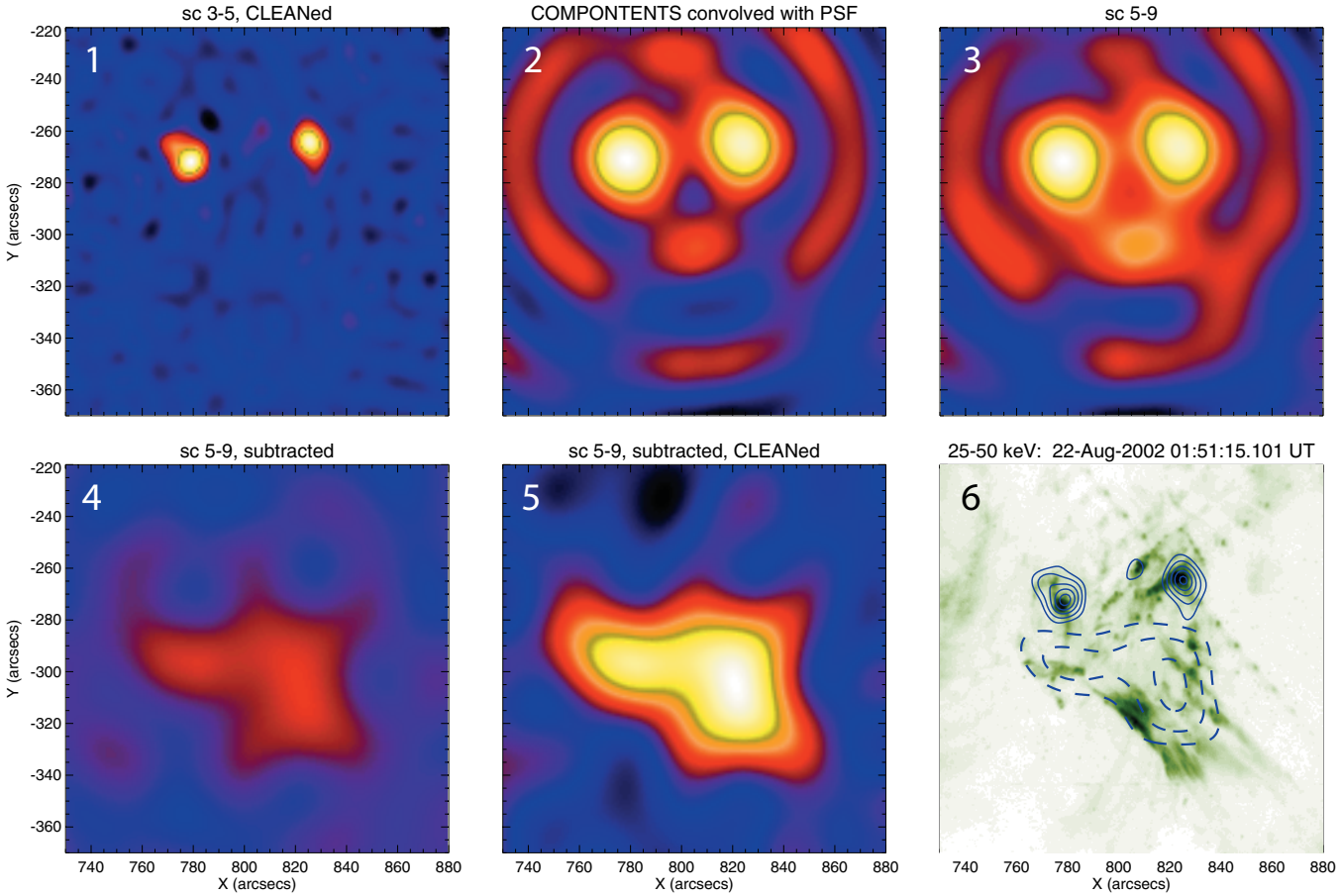


**Figure 6.** "Two-step-clean" algorithm applied to the event of 2002 August 22 integrated from 01:50:45 to 01:51:45 UT. (1) The CLEANed fine-resolution image reconstructed in the energy range 25–50 keV using subcollimators 3–5. (2) The CLEAN components from the CLEANed image shown to the left convolved with the *RHESSI* point-spread function using coarse subcollimators 5–9 only. (3) Low-resolution backprojection image using subcollimator 5–9. (4) The same backprojection image with the CLEAN components of the compact sources convolved with the point-spread function subtracted. (5) The CLEANed image of the residual map. (6) The footpoint emission (blue contours) and the extended coronal source (dashed blue contours) plotted on the *TRACE* image from 01:51:19 UT.

(A color version of this figure is available in the online journal.)

coronal source (maximal 5.3% of the brightest footpoint), the extended area makes the total flux of the coronal source of the same order as the footpoint flux. We analyzed our set of 16 events in the same way, but none of the events shows a coronal source as in the event of Bain & Fletcher (2009). A more detailed investigation including time variations should be done in the future. However, it is noted here, that the jet discussed by Bain & Fletcher (2009) is a different kind of event than the jets discussed in this paper. (1) The associated flare is a two-ribbon flare associated with a gradual solar energetic particle event with a different geometry as the interchange reconnection scenario discussed here. (2) The associated electron event seen at 1 AU is a delayed event and not a prompt event as selected for our study. (3) The EUV jet is much more complex than the jets associated with the events presented here. Therefore, we do not necessarily expect to observe the same hard X-ray signature for our set of events.

## 3. SUMMARY AND DISCUSSIONS

Our statistical survey corroborates that the interchange reconnection topology is the most common origin of prompt solar energetic electron events seen at 1 AU (Figure 7). Because not all events in our sample show three hard X-ray footpoints, we cannot exclude that other magnetic topologies are possible in the production of escaping electrons as well.

One striking observational fact is the much larger number of accelerated deka-keV electrons seen in the chromospheric footpoints compared to number of escaping electrons (for details on how these order-of-magnitude estimates are derived we refer to Lin & Hudson 1971). Neither Coulomb collisions nor wave-particle interactions can account for this large difference. While electrons of a few keV energy are likely to lose all their energy to Coulomb collisions before escaping the corona (e.g., Lin 1985; Saint-Hilaire et al. 2009), electrons above 10 keV should be able to escape to the interplanetary medium. For a fast type III burst exciter speed around the third of the speed of light, the corresponding electron energies are around ~30 keV. Hence, wave-particle interactions modify the spectrum of electrons below this threshold energy, but electrons with higher energies are generally not affected.

An asymmetric acceleration efficiency in the up–down direction could be the result of acceleration in a collapsing trap (e.g., Karlický & Kosugi 2004). Energetic electrons within the flare loop could undergo acceleration by the betatron process, as the newly reconnected loop collapses. However, it is unclear why the third footpoint source would be as bright as the footpoints in the closed loop. Minoshima et al. (2010) suggest that two types of acceleration are simultaneously at work: the inertia drift acceleration is responsible for escaping electrons, while the betatron acceleration enhances the electron velocity

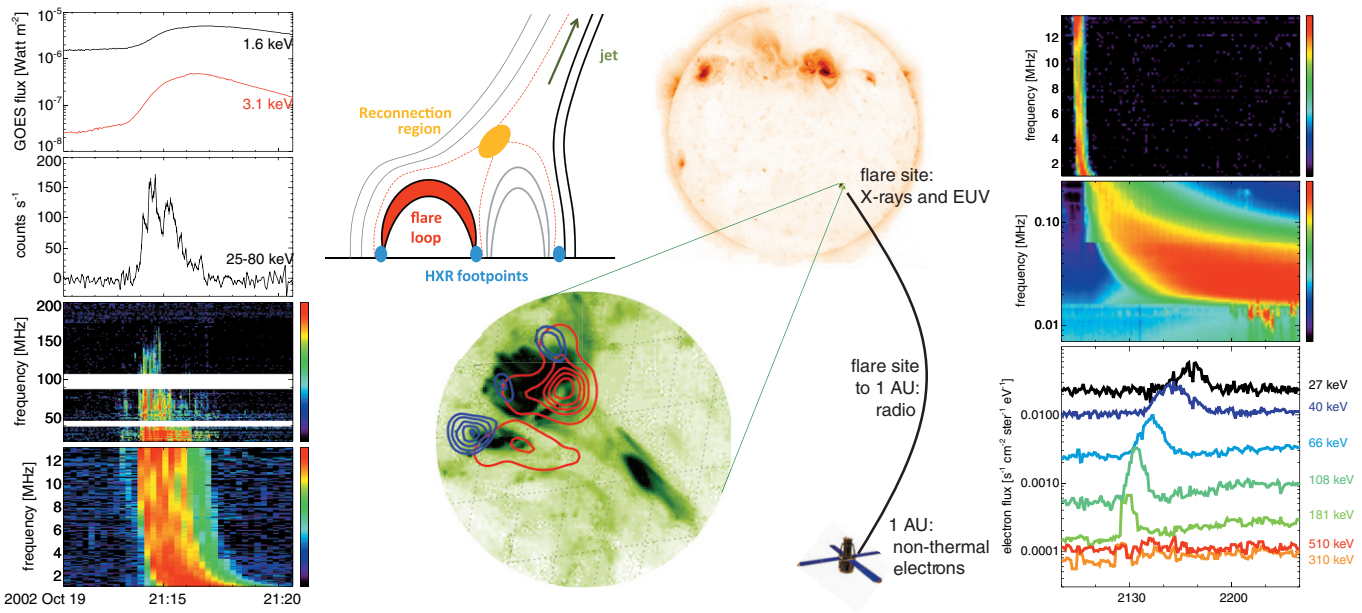


**Figure 7.** Schematic describing prompt solar energetic electron events. Left and right: time series in soft and hard X-rays, radio waves, and non-thermal electrons seen near 1 AU track energetic electrons from their acceleration site at the Sun into interplanetary space. Center: hard X-ray and EUV imaging results of the source region are shown together with a schematic of interchange reconnection. The reconnection region, the flare loop, the hard X-ray footpoints, and the jet are labeled. The red dashed lines give the field lines that are currently reconnecting. Previously reconnected field lines are shown in black, while the field lines next to reconnect are given in gray.

(A color version of this figure is available in the online journal.)

perpendicular to the magnetic field and energizes the bulk of flare electrons. However, also in this model it is unclear why the number of escaping electrons is so much smaller than the number of electrons precipitating along the open field line.

Brown et al. (2009) and Turkmani & Brown (2010) have recently proposed a flare model involving local re-acceleration. In their scenario, electrons gain energy in electric fields from cascading current sheets that occur within the entire flare loop including the footpoints (Vlahos et al. 2004; Turkmani et al. 2006). Because the acceleration efficiency scales with magnetic field strength, acceleration is strongest within the chromospheric footpoint. Hence, within the hard X-ray source region, electrons not only lose energy by collisions, but also gain energy (i.e., electrons are locally re-accelerated). Compared to the thick target model, the re-acceleration scenario therefore requires fewer electrons to produce the same hard X-ray emission (note that the required total energy remains the same). Re-acceleration of escaping electrons is expected to be much less efficient because of the low magnetic field strength in the corona. Hence, a local re-acceleration model could, in principle, explain the low number of escaping electrons. However, this model does not make specific prediction that can be compared with the observations. While the test particle approach employed by Brown et al. (2009) is useful to estimate the re-acceleration rate, it does not explain how the cascading current sheets evolve in time in response to particle energetization and finally saturate.

The low number of escaping electrons could also be explained by all the models where the main acceleration occurs in the chromospheric footpoints (e.g., Fletcher & Hudson 2008). In this case, the escape efficiency from the chromospheric acceleration region would give the fraction of escaping electrons. However, the details of the acceleration process in footpoints nor the escape from the footpoints are currently understood.

Future analysis of this type of imaging data sets should focus on the time evolution. *SDO* provides ~10 s cadence data of full-disk images at multiple EUV wavelengths, a significant improvement compared to the data shown in Figure 4. *RHESSI* imaging observations can easily match this cadence. The addition of *STEREO* observations will provide different view angles of the flare site and in situ electron observations for events not magnetically connected to Earth. This will greatly enhance the number of events with a complete set of observations. The breakthrough in understanding of electron acceleration and transport, however, is expect with the launch of inner heliospheric missions such as Solar Orbiter, Solar Probe Plus, and Interhelio-Probe currently planned to be launched in the time frame of 2017 to 2018.

We thank the referee for carefully reading our paper. The work was supported through NASA contract NAS 5-98033 for *RHESSI* and grant NNG 05GH18G for *WIND*. E.P.K. gratefully acknowledges the support of a PPARC Advanced Fellowship and STFC Rolling grant.

## REFERENCES

Aschwanden, M. J., Wülser, J.-P., Nitta, N. V., & Lemen, J. R. 2008, ApJ, 679, 827
Aurass, H., Klein, K.-L., & Martens, P. C. H. 1994, Sol. Phys., 155, 203
Axford, W. I., & McKenzie, J. F. 1992, Solar Wind Seven (COSPAR Colloquia Ser. 3), ed. E. Marsch & R. Schwenn (Oxford: Pergamon), 1
Bain, H. M., & Fletcher, L. 2009, A&A, 508, 1443
Baker, D., Rouillard, A. P., van Driel-Gesztelyi, L., et al. 2009, Ann. Geophys., 27, 3883
Benz, A. O. 2008, Living Rev. Sol. Phys., 5, 1
Benz, A. O., Grigis, P. C., Csillaghy, A., & Saint-Hilaire, P. 2005, Sol. Phys., 226, 121
Benz, A. O., Lin, R. P., Sheiner, O. A., Krucker, S., & Fainberg, J. 2001, Sol. Phys., 203, 131

Bougeret, J.-L., Kaiser, M. L., Kellogg, P. J., et al. 1995, Space Sci. Rev., 71, 231
Brown, J. C., Turkmani, R., Kontar, E. P., MacKinnon, A. L., & Vlahos, L. 2009, A&A, 508, 993
Chifor, C., Isobe, H., Mason, H. E., et al. 2008, A&A, 491, 279
Christe, S., Krucker, S., & Lin, R. P. 2008, ApJ, 680, L149
Cirtain, J. W., Golub, L., Lundquist, L., et al. 2007, Science, 318, 1580
Cranmer, S. R., & van Ballegooijen, A. A. 2010, ApJ, 720, 824
Crooker, N. U., & Webb, D. F. 2006, J. Geophys. Res. (Space Phys.), 111, A08108
Dennis, B. R., Emslie, A. G., & Hudson, H. S. 2011, Space Sci. Rev., 155
Dennis, B. R., & Pernak, R. L. 2009, ApJ, 698, 2131
Fisk, L. A. 2003, J. Geophys. Res. (Space Phys.), 108, 1157
Fletcher, L., & Hudson, H. S. 2008, ApJ, 675, 1645
Ginzburg, V. L., & Zheleznyakov, V. V. 1958, SvA, 2, 653
Haggerty, D. K., & Roelof, E. C. 2002, ApJ, 579, 841
Handy, B. N., Acton, L. W., Kankelborg, C. C., et al. 1999, Sol. Phys., 187, 229
Hoyng, P., Duijveman, A., Machado, M. E., et al. 1981, ApJ, 246, L155
Hudson, H. S., Kosugi, T., Nitta, N. V., & Shimojo, M. 2001, ApJ, 561, L211
Hurford, G. J., Schmahl, E. J., Schwartz, R. A., et al. 2002, Sol. Phys., 210, 61
Kane, S. R. 1981, ApJ, 247, 1113
Kane, S. R., McTiernan, J., Loran, J., et al. 1992, ApJ, 390, 687
Karlický, M., & Kosugi, T. 2004, A&A, 419, 1159
Kim, Y.-H., Moon, Y.-J., Park, Y.-D., et al. 2007, PASJ, 59, 763
Klassen, A., Bothmer, V., Mann, G., et al. 2002, A&A, 385, 1078
Klein, K.-L., Krucker, S., Lointier, G., & Kerdraon, A. 2008, A&A, 486, 589
Klein, K.-L., Krucker, S., Trottet, G., & Hoang, S. 2005, A&A, 431, 1047
Krucker, S., Battaglia, M., Cargill, P. J., et al. 2008, A&AR, 16, 155
Krucker, S., Hudson, H. S., Jeffrey, N. L. S., et al. 2011, ApJ, 739, 96
Krucker, S., Kontar, E. P., Christe, S., & Lin, R. P. 2007a, ApJ, 663, L109
Krucker, S., Larson, D. E., Lin, R. P., & Thompson, B. J. 1999, ApJ, 519, 864
Krucker, S., & Lin, R. P. 2008, ApJ, 673, 1181
Krucker, S., Saint-Hilaire, P., Christe, S., et al. 2008, ApJ, 681, 644
Krucker, S., White, S. M., & Lin, R. P. 2007b, ApJ, 669, L49
Kundu, M. R., Raulin, J. P., Nitta, N., et al. 1995, ApJ, 447, L135
Lin, R. P. 1985, Sol. Phys., 100, 537
Lin, R. P., Anderson, K. A., Ashford, S., et al. 1995, Space Sci. Rev., 71, 125
Lin, R. P., Dennis, B. R., Hurford, G. J., et al. 2002, Sol. Phys., 210, 3
Lin, R. P., & Hudson, H. S. 1971, Sol. Phys., 17, 412
Liu, C., Lee, J., Gary, D. E., & Wang, H. 2007, ApJ, 658, L127
Masuda, S., Kosugi, T., & Hudson, H. S. 2001, Sol. Phys., 204, 55
Melrose, D. B. 1990, Sol. Phys., 130, 3
Minoshima, T., Masuda, S., & Miyoshi, Y. 2010, ApJ, 714, 332
Muschietti, L. 1990, Sol. Phys., 130, 201
Nitta, N. V., Mason, G. M., Wiedenbeck, M. E., et al. 2008, ApJ, 675, L125
Parker, E. N. 1973, ApJ, 180, 247
Pick, M., Mason, G. M., Wang, Y.-M., Tan, C., & Wang, L. 2006, ApJ, 648, 1247
Qiu, J., Lee, J., Gary, D. E., & Wang, H. 2002, ApJ, 565, 1335
Raulin, J. P., Kundu, M. R., Nitta, N., & Raoult, A. 1996, ApJ, 472, 874
Saint-Hilaire, P., Krucker, S., Christe, S., & Lin, R. P. 2009, ApJ, 696, 941
Savcheva, A., et al. 2007, PASJ, 59, 771
Scherrer, P. H., Bogart, R. S., Bush, R. I., et al. 1995, Sol. Phys., 162, 129
Schmahl, E. J., Pernak, R. L., Hurford, G. J., Lee, J., & Bong, S. 2007, Sol. Phys., 240, 241
Shibata, K., Ishido, Y., Acton, L. W., et al. 1992, PASJ, 44, L173
Shimojo, M., Hashimoto, S., Shibata, K., et al. 1996, PASJ, 48, 123
Smith, D. M., Share, G. H., Murphy, R. J., et al. 2003, ApJ, 595, L81
Turkmani, R., & Brown, J. 2010, arXiv:1011.0756
Turkmani, R., Cargill, P. J., Galsgaard, K., Vlahos, L., & Isliker, H. 2006, A&A, 449, 749
Vlahos, L., Isliker, H., & Lepreti, F. 2004, ApJ, 608, 540
Wang, L., Lin, R. P., Krucker, S., & Gosling, J. T. 2006a, Geophys. Res. Lett., 33, 3106
Yang, Y.-H., Cheng, C. Z., Krucker, S., Lin, R. P., & Ip, W. H. 2009, ApJ, 693, 132
Wang, Y.-M., Pick, M., & Mason, G. M. 2006b, ApJ, 639, 495
Wang, Y.-M., & Sheeley, N. R., Jr. 2002, ApJ, 575, 542
Zaitsev, V. V., Mityakov, N. A., & Rapoport, V. O. 1972, Sol. Phys., 24, 444
Zharkova, V. V., Arzner, K., Benz, A. O., et al. 2011, Space Sci. Rev., 156